

# Operator learning for models of tear film breakup

Qinying Chen<sup>1</sup>, Arnab Roy<sup>1†</sup>, Tobin A. Driscoll<sup>1†</sup>

<sup>1</sup>Department of Mathematical Sciences, University of Delaware,  
Newark, 19716, DE, USA.

Contributing authors: [cqyzxy@udel.edu](mailto:cqyzxy@udel.edu); [arnabroy@udel.edu](mailto:arnabroy@udel.edu);  
[driscoll@udel.edu](mailto:driscoll@udel.edu);

<sup>†</sup>These authors contributed equally to this work.

## Abstract

Tear film (TF) breakup is a key driver of understanding dry eye disease, yet estimating TF thickness and osmolarity from fluorescence (FL) imaging typically requires solving computationally expensive inverse problems. We propose an operator learning framework that replaces traditional inverse solvers with neural operators trained on simulated TF dynamics. This approach offers a scalable path toward rapid, data-driven analysis of tear film dynamics.

**Keywords:** Tear film, dry eye disease, fluorescent imaging, scientific machine learning, operator learning

**MSC:** 92C35

## 1 Introduction

A thin layer of liquid known as the tear film (TF) lies across the surface of the cornea of a human eye [1]. This dynamic film provides lubrication, protects against microbial invasion, maintains a smooth optical interface, and delivers essential oxygen and nutrients to the cornea [2]. The TF has three layers: a lipid layer that is 20 to 100 nm thick [3], an aqueous layer consisting mainly of water [4] that is a few microns thick, and a half-micron thick mucin layer called the glycocalyx that is on the ocular surface [5]. The lipid layer slows evaporation of water from the TF [6], and a healthy glycocalyx facilitates the fluid movements of the ocular surface [7]. The lacrimal gland supplies the majority of the water from the aqueous layer near the temporal canthus [8]. Osmosis supplies water from the ocular epithelia [9].

When the tear film becomes unstable and breaks up, a process known as tear breakup (TBU), it can leave patches of the ocular surface exposed, triggering irritation, inflammation, and visual disturbances [10]. Persistent or frequent tear breakup is recognized as a major factor in the onset and progression of dry eye disease (DED), a multifactorial condition affecting millions of individuals worldwide that compromises both the comfort and visual function of the eye [11–13]. One common subtype, evaporative dry eye (EDE), is primarily driven by excessive water loss from the tear film, often due to dysfunction in the lipid layer that normally retards evaporation [14, 15]. TBU happens when a dry spot appears on the eye [16] and is often evaporation-driven [2, 11].

Measurement of TF dynamics *in situ* is challenging. Evaporation has been identified as a primary driver, with models incorporating spatially varying lipid layers, osmolarity transport in the aqueous layer, and osmosis across the cornea [3, 17, 18]. These studies showed that osmolarity diffusion prevents osmosis from halting thinning, a phenomenon absent in spatially uniform models [9]. Simpler models later included fluorescein transport, enabling direct comparison with imaging experiments, and one-dimensional PDE frameworks have combined evaporation and fluorescein dynamics to estimate otherwise unmeasurable parameters [19–21]. More recently, spatially independent ODE models have been calibrated to small TBU spots and streaks and coupled with neural-network–based data extraction to expand datasets [22, 23]. Additional work has addressed evaporation dynamics and instability mechanisms [24, 25].

While the results of [23] are an important first step toward a complete understanding of TF dynamics, they are limited on one hand by the relative crudeness of the mathematical model and on the other hand by the need to computationally solve an inverse problem for each prospective TBU location. While fully 2D PDE model simulation has been established [26] and simple inverse problems for the 2D model have been demonstrated for isolated TBU cases [27], solving the 2D inverse problem at large scale is currently computationally expensive.

In this work, we investigate operator learning techniques [28–31] to ODE and 1D PDE models of TBU dynamics. In operator learning, one trains a deep neural network or other learning architecture to the outputs of a simulation as its inputs vary widely over the domain of its parameter space. In our context, the goal is to build a mapping directly from observations, in the form of synthetic FL imaging data, to outcomes, in the form of TF thickness and osmolarity functions, without the need to simulate the physics or solve an inverse problem. If successful, this process provides a fast computational method that could be used in real time to predict characteristics of tear film flows from FL imaging. At the modeling level, we can compare the results of predictors trained on ODE and PDE models to clarify how often and under what circumstances they make substantially different predictions.

In [section 2](#) we describe the ODE and PDE models used to simulate TF dynamics during TBU. In [section 3](#) we describe three operator learning methods that are used and tested. In [section 4](#) we present the results of numerical experiments with the two simulation models and operator learning methods, and in [section 5](#) we make concluding remarks and observations.

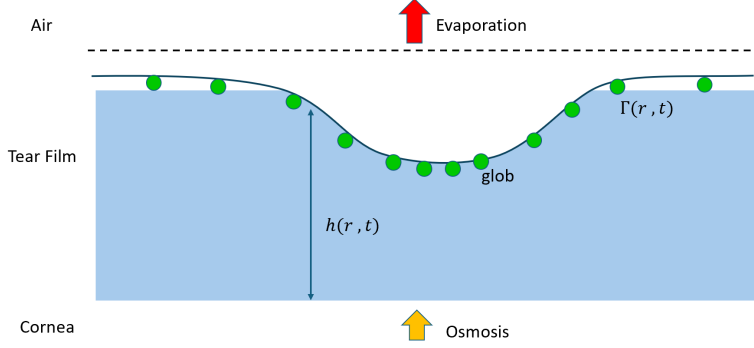


**Fig. 1:** Mechanisms in the tear film at a later time  $t > 0$ . Evaporation occurs at the top, osmosis at the bottom;  $\Gamma$  represents the surfactant concentration, and  $h$  represents the tear film thickness.

## 2 Mathematical models

### 2.1 One-dimensional PDE

The PDE system is derived from [19] and describes the situation depicted in Figure 1 of a radially symmetric glob of lipid on top of the aqueous layer at a later time  $t > 0$ . The dashed line in the picture represents the tear film at  $t = 0$ . We assume there is nonzero constant evaporation under the glob and zero evaporation outside the glob. The Marangoni effect, driven by tangential flow, arises in regions where thicker globs of the lipid layer are present. These areas, with higher surfactant concentration, reduce the aqueous/air surface tension and trigger fluid motion along the surface, leading to rapid film breakup. We expect that diffusion, advection, evaporation, osmosis, and Marangoni flow together influence the TF thickness which would result in TBU.

The independent and dependent variables are shown in Table 1. Quantities named without primes are nondimensionalized according to

$$\begin{aligned} r' &= \ell r, & z' &= h'_0 z, & t' &= t'_s t, & h' &= h'_0 h, & u'_r &= U u_r, \\ p' &= \frac{\mu U}{\ell \epsilon^2} p, & \Gamma' &= \Gamma_0 \Gamma, & J' &= \epsilon \rho U J, & c' &= c_0 c, & f' &= f_{\text{cr}} f, & f'_0 &= f_{\text{cr}} f_0 \end{aligned}$$

where primes denote dimensional quantities and the relevant physical parameters are given in Table 2. The nondimensional parameters are shown in Table 3.

The resulting nondimensional PDE system for the dependent variables  $h$ ,  $p$ ,  $c$ ,  $\Gamma$  and  $f$  is

$$\partial_t h = -J + P_c(c - 1) - \frac{1}{r} \partial_r(r h \bar{u}), \quad (1a)$$

$$p = -\frac{1}{r} \partial_r(r \partial_r h) - A h^{-3}, \quad (1b)$$

Variable	Meaning
$r$	spot radius
$z$	depth dimension
$t$	time
$\Gamma(r, t)$	lipid surfactant concentration
$u_r(r, h, t)$	Horizontal surface fluid velocity
$h(r, t)$	TF thickness
$p(r, t)$	pressure
$J(r)$	evaporation rate
$c(r, t)$	osmolarity
$f(r, t)$	fluorescein concentration

**Table 1:** Variables in the 1D glob model.

Parameter	Description	Value	Reference
$\mu$	Viscosity	$1.3 \times 10^{-3} \text{ Pa sec}$	Tiffany [32]
$\sigma_0$	Surface tension	$0.045 \text{ N m}^{-1}$	Nagyová and Tiffany [33]
$\rho$	Density	$10^3 \text{ kg m}^{-3}$	Water
$A^*$	Hamaker Constant	$6\pi \times 3.5 \times 10^{-19} \text{ S m}^{-1}$	Ajaev and Homsy [34]
$h_0$	Initial TF thickness	$2 \mu\text{m}$ to $8 \mu\text{m}$	Calculated
$(\Delta\sigma)_0$	Change in surface tension	$2 \mu\text{N m}^{-1}$ to $60 \mu\text{N m}^{-1}$	Calculated
$t_s$	Observation timescale	10 sec to 60 sec	Calculated
$v$	Thinning rate	$0 \mu\text{m min}^{-1}$ to $40 \mu\text{m min}^{-1}$	Calculated
$f_0$	Initial FL concentration	0.08 % to 0.2 %	Calculated
$R_I$	Glob radius	0.02 mm to 0.2 mm	Calculated
$V_w$	Molar volume of water	$1.8 \times 10^{-5} \text{ m}^3 \text{ mol}^{-1}$	Water
$D_f$	Diffusivity of fluorescein	$0.39 \times 10^{-9} \text{ m}^2/\text{sec}$	Casalini et al. [35]
$D_o$	Diffusivity of salt	$1.6 \times 10^{-9} \text{ m}^2/\text{sec}$	Riquelme et al. [36]
$c_0$	Isotonic osmolarity	$300 \text{ Osm m}^{-3}$	Lemp et al. [37]
$P_0$	Permeability of cornea	$12.1 \mu\text{m/sec}$	Braun et al. [3]
$\ell$	Characteristic length, $(t_s \sigma_0 h_0^3 / \mu)^{1/4}$	0.138 mm to 0.412 mm	Calculated
$U$	Characteristic velocity, $(\sigma_0 h_0^3 / \mu t_s^3)^{1/4}$	0.056 mm/sec to 0.099 mm/sec	Calculated
$\epsilon_f$	Napierian extinction coefficient	$1.75 \times 10^7 \text{ L m}^{-1} \text{ mol}^{-1}$	Mota et al. [38]
$f_{cr}$	Critical FL concentration	0.2%	Webber and Jones [39]

**Table 2:** Physical parameters (dimensional) used in the governing equations.

Parameter	Description	Expression
$\epsilon$	Aspect ratio	$h_0'/\ell$
$M$	Marangoni number	$\epsilon(\Delta\sigma)_0 [t_s^{1/3} / (\sigma_0 \mu^3 h_0'^3)]^{1/4}$
$A$	Non-dimensional Hamaker constant	$A^* / [\epsilon(\Delta\sigma)_0 h_0' \ell]$
$P_c$	Permeability of cornea	$(P_0 V_w c_0) / (\epsilon U)$
$\text{Pe}_f$	Péclet number for FL diffusion	$U \ell / D_f$
$\text{Pe}_c$	Péclet number for salt ion diffusion	$U \ell / D_o$
$\text{Pe}_s$	Péclet number for surface diffusion	$\epsilon(\Delta\sigma)_0 \ell / (\mu D_s)$
$\phi$	Non-dimensional Napierian extinction coefficient	$\epsilon f_{cr} h_0'$

**Table 3:** Non-dimensional parameters used in the governing equations.

$$\partial_t \Gamma = \left[ \text{Pe}_s^{-1} \left( \frac{1}{r} \partial_r (r \partial_r \Gamma) \right) - \frac{1}{r} \partial_r (r u_r \Gamma) \right] B, \quad (1c)$$

$$h(\partial_t c + \bar{u} \partial_r c) = \text{Pe}_c^{-1} \left( \frac{1}{r} \partial_r (r h \partial_r c) \right) + Jc - P_c(c-1)c \quad (1d)$$

$$h(\partial_t f + \bar{u} \partial_r f) = \text{Pe}_f^{-1} \left( \frac{1}{r} \partial_r (r h \partial_r f) \right) + Jf - P_c(c-1)f, \quad (1e)$$

where  $B$  is a smooth approximation to a transition step function,

$$B(r, R_I) = \frac{1}{2} + \frac{1}{2} \tanh \left( \frac{r - R_I}{0.1} \right),$$

and the horizontal surface TF fluid velocity  $u_r(r, h, t)$  and average horizontal TF fluid velocity  $\bar{u}$  throughout the film are given by

$$u_r(r, h, t) = -\frac{\frac{1}{2}h^2(\partial_r p)B + M\partial_r \Gamma h B}{B + (1 - B)h}, \quad (2)$$

$$\bar{u} = -\frac{\frac{1}{3}h^2(\partial_r p)[B + \frac{1}{4}h(1 - B)] + \frac{1}{2}M\partial_r \Gamma h B}{B + (1 - B)h}. \quad (3)$$

In order to simulate the effect of the lipid glob on evaporation, we define the dimensional evaporative flux by

$$J'(r) = \rho'(1 - B(r))v'.$$

Since we are not interested in boundary effects such as eyelids, we assume periodic conditions on all the dependent variables and that all the dependent variables are initially uniform:

$$h(r, 0) = c(r, 0) = 1, \quad f(r, 0) = f_0, \quad (4)$$

where  $f_0$  is the FL concentration normalized to the critical concentration  $f_{\text{cr}}$ . Once  $h$  and  $f$  are known, we compute the FL intensity via [39, 40]

$$I = I_0 \frac{1 - \exp(-\phi f h)}{1 + f^2}, \quad (5)$$

where  $I_0$  is a normalization coefficient so that  $I(0) = 1$  and  $\phi$  is the nondimensional Napierian extinction coefficient.

The values of  $h'_0$ ,  $t'_s$ , and  $f'_0$  are determined for each FL trial by the methods described in [41], and we consider them as being provided to the model. The glob radius  $R'_I$ , surface tension change  $(\Delta\sigma)'_0$ , and nominal thinning rate  $v'$  are additional parameters to the model. Hence, there is a 6-dimensional parameter space affecting the output of the model.

For discretization, we use the method of lines with a Fourier spectral collocation method [42] in space on a uniform periodic grid and exploit symmetry by solving over  $r \in (0, \pi]$ . The resulting discretization of spatial terms in (1a)–(1e) creates a

differential-algebraic system (DAE) that is solved in Julia using the Rodas5P solver, a 5th order A-stable stiffly stable Rosenbrock method in the **DifferentialEquations** package [43]. Computations were performed using Julia version 1.10.5 on a Windows laptop with a 12th Gen Intel Core i7-12700H 2.30GHz processor and 32GB RAM.

## 2.2 ODE

To simplify the model (1), we follow the procedure in [23] to remove the spatial dependence and model only at the glob center. In order to replace the tangential flow caused by surface tension gradients that are no longer possible, we impose a time-dependent shear stress term

$$g(t) = b'_1 e^{-b'_2 t}, \quad (6)$$

for dimensional parameters  $b'_1$ , the maximum shear, and  $b'_2 \geq 0$ , the decay constant. When  $b'_1 > 0$ , the film thins as though there is outward flow from the center of the glob, while  $b'_1 < 0$  causes thickening from an inward flow. Because there can no longer be diffusion, the only difference between osmolarity  $c(t)$  and fluorescein concentration  $f(t)$  is a constant of proportionality, so  $f$  is dropped as a dependent variable. In addition, we assume a constant evaporation rate  $J'_e$ . Then we nondimensionalize the parameters and variables according to the following relations:

$$J_e = \frac{J'_e t'_s}{h'_0}, \quad f_0 = \frac{f'_0}{f_{\text{cr}}}, \quad b_1 = b'_1 t'_s, \quad b_2 = b'_2 t'_s$$

where  $f_{\text{cr}} = 5.3 \times 10^{-3}$  % is the critical fluorescence concentration.

The resulting system, in nondimensional form, is

$$\frac{dh}{dt} = P_c(c - 1) - g(t)h - J, \quad (7a)$$

$$h \frac{dc}{dt} = -g(t)hc - \frac{dh}{dt}c, \quad (7b)$$

$$h(0) = 1, \quad (7c)$$

$$c(0) = 1. \quad (7d)$$

This model was labeled as Model D in [23]. Once  $h$  and  $c$  are computed,  $f(t)$  is found via  $f(t) = f_0 c(t)$ . The FL intensity  $I$  is again given by (5).

The dimensional parameters for (7) again include the initial thickness  $h'_0$ , the trial time  $t'_s$ , the initial fluorescein concentration,  $f'_0$ , and the thinning rate  $J'_e$ , as in the PDE model. However, the glob radius and surface tension parameters are replaced by the constants  $b'_1$  and  $b'_2$  in (6).

## 3 Operator learning models

Each of the mathematical models in section 2 effectively maps a parameter space to physically relevant outputs for nondimensional (i.e., relative) thickness  $h$ , osmolarity

$c$ , and the observed FL intensity  $I$ . In practice, our goal is to map an observed time series for  $I(t)$  to the thickness and osmolarity functions. Using a mathematical model, this can be treated as an inverse problem, using an observation to find the best-fit parameters of the model, whose solution provides  $h$  and  $c$ .

Instead, we can use operator learning [28] to train a machine learning method to produce the  $I \mapsto (h, c)$  mapping directly, without solving or even referring to a mathematical model. This approach offers the possibility of using model solutions solely to produce training data. After the training is complete, the learner can make predictions very quickly. In addition, by training learners on different mathematical models, we can assess to what extent, and for which observations, one model produces results similar to the other.

There are many forms of operator learning in the literature, using different ways to represent the input and output spaces as well as the connection between them. We report results for three approaches: Fourier feature networks (FFN), dense neural networks between spaces that are compressed via principal components analysis (Dense-PCA), and dense networks with inputs that enhance PCA inputs with externally known parameters (Dense-PCAX).

### 3.1 Generation of training/testing data

The ODE and PDE models of section 2 were used to generate two synthetic datasets for training and testing the ML models. Each begins by sampling parameters using six-dimensional Halton sequences within the ranges given in Table 4. Because it is not straightforward to *a priori* characterize which parameters produce physically and physiologically reasonable results, we reject simulations that have any of the following characteristics:

*Upper bound on thickness.* Instances where  $h(t) > 1.1$  at any time were discarded, as tear film thickness is generally expected to decrease at the start of simulation time.

*Lower bound on thickness.* Solutions where  $h(t) < 0.2$  were excluded, since different dynamics will hold when the thickness of the film is comparable to the glycocalyx thickness.

*Nonphysical growth.* Instances with  $h(1) > 1.5 \min h(t)$  were removed to rule out nonphysical regrowth after an initial thinning phase.

*Increasing intensity.* We collect data only with decreasing fluorescence intensity over time, so instances where  $I(t)$  increases were discarded.

The surviving cases constitute a parameter set  $\Omega \subset \mathbf{R}^6$ .

Each element of  $\Omega$  is associated with resulting solutions for  $c$ ,  $h$ , and  $I$ . For the ODE, each variable is a function of time only and was sampled at  $N = 601$  equally spaced times; for the PDE, each was sampled at  $N$  equally spaced times and  $r = 0$ , which is the center of the glob. These discretizations produced the realization sets  $\mathcal{C}$ ,  $\mathcal{H}$ , and  $\mathcal{I}$ , all subsets of  $\mathbf{R}^N$ . The elements of  $\mathcal{I}$  were used as input feature vectors mapping to corresponding output feature vectors from either  $\mathcal{C}$  or  $\mathcal{H}$ . (It would also be possible to concatenate corresponding elements of  $\mathcal{C}$  and  $\mathcal{H}$  and train a single learner to produce both outputs simultaneously, but that possibility was not explored for this work.) For the PDE model,  $|\mathcal{I}| = 28698$ , while for the ODE model,  $|\mathcal{I}| = 64522$ .

Parameter	ODE		PDE	
	Range		Range	
$h'_0$	[2 $\mu\text{m}$ , 8 $\mu\text{m}$ ]		$h'_0$	[2 $\mu\text{m}$ , 8 $\mu\text{m}$ ]
$f'_0$	[0.08 %, 0.2 %]		$f'_0$	[0.08 %, 0.2 %]
$t'_s$	[10 sec, 60 sec]		$t'_s$	[10 sec, 60 sec]
$v'$	[0 $\mu\text{m min}^{-1}$ , 40 $\mu\text{m min}^{-1}$ ]		$J'_e$	[0 $\mu\text{m min}^{-1}$ , 40 $\mu\text{m min}^{-1}$ ]
$R'_I$	[0.02 mm, 0.2 mm]		$b_1$	[−0.2 $\text{sec}^{-1}$ , 2.0 $\text{sec}^{-1}$ ]
$(\Delta\sigma)'_0$	[2 $\mu\text{N m}^{-1}$ , 60 $\mu\text{N m}^{-1}$ ]		$b_2$	[0 $\text{sec}^{-1}$ , 2.0 $\text{sec}^{-1}$ ]

**Table 4:** Ranges for dimensional parameters used to create synthetic datasets for ML training. See [Section 2](#) for their roles in the mathematical models.

In order to improve the robustness of predictions for noisy experimental observations, we augmented the input set with copies that were randomly perturbed by multiplicative noise. To make perturbations similar to those observed in the experimental dataset, the noise for a signal vector  $I$  is a Gaussian-smoothed ( $\sigma = 9$ ) white noise of standard deviation  $0.25|I_1 - I_N|$ . Two perturbed copies of each input vector (and clean copies of the corresponding outputs) were added to  $\mathcal{I}$ , which was then split into training and testing subsets  $\mathcal{I}_{\text{tr}}$  (75%) and  $\mathcal{I}_{\text{te}}$  (25%), respectively, along with the corresponding outputs.

### 3.2 Fourier feature network (FFN)

A Fourier feature network (FFN) uses an input layer of randomized linear combinations of Fourier modes of the input features to reduce dimensionality while retaining the ability to learn of functions with fine-scale variations [\[44\]](#). Our FFN comprises an input layer, three hidden layers with ReLU activation, and an output layer:

$$\hat{y} = f(\gamma(I)) = W_4 \sigma(W_3 \sigma(W_2 \sigma(W_1 \gamma(I) + v_1) + v_2) + v_3) + v_4.$$

Here,  $\gamma(I)$  denotes the Fourier feature mapping, defined as

$$\gamma(I) = [\sin(2\pi\sigma_j I), \cos(2\pi\sigma_j I)]_{j=1}^3,$$

where  $I$  is the  $N$ -dimensional input vector and  $\sigma_j \in \{0.5, 1, 2\}$  represents frequency scales selected to capture varying resolution details. This makes  $\gamma(I)$  an array of length  $6N$ . The hidden layers are dense networks with weight matrices  $W_i$  and bias vectors  $v_i$  for  $i = 1, 2, 3$ , and  $W_4$  and  $v_4$  characterize the dense output layer to produce a time series prediction of length  $N$  for either  $c$  or  $h$ .

The first weight matrix  $W_1$  has shape  $300 \times 6N$  and the bias vector  $v_1$  has length 300. The next two hidden layers have weight matrices of sizes  $200 \times 300$  and  $200 \times 200$ , with corresponding bias vectors. After each of the first three layers, the activation function  $\sigma = \text{ReLU}$  is applied. The last weight matrix  $W_4$  of the output layer has size  $N \times 200$  to produce a time series of either  $c$  or  $h$ .

Training was performed using the mean squared error (MSE) loss with a smoothness regularization:

$$\mathcal{L}(y - \hat{y}) = \frac{1}{N} \sum_{t=1}^N (y_t - \hat{y}_t)^2 + \frac{\alpha}{N-1} \sum_{t=1}^{N-1} (\hat{y}_{t+1} - \hat{y}_t)^2. \quad (8)$$

The regularization term is used to suppress high-frequency oscillations, since the output  $\hat{y}$  is meant to represent a time series from a dynamical system with smooth solutions. We chose  $\alpha = 1.6$  as the regularization parameter.

### 3.3 Dense neural network with PCA (Dense-PCA)

Another way to encode the input and output time series is to apply PCA to them, connecting the coefficient spaces by a fully-connected neural network [45]. Reducing dimensionality reduces the number of training parameters and may help focus attention on the most salient features of the signals.

The fully connected neural networks used three hidden layers of 300 neurons with ReLU activation:

$$x = P(I - \mu) \quad (9)$$

$$\hat{y} = \nu + Q[W_4 \sigma(W_3 \sigma(W_2 \sigma(W_1 x + v_1) + v_2) + v_3) + v_4], \quad (10)$$

where  $(P, \mu)$  and  $(Q, \nu)$  denote PCA compression and reconstruction, respectively, and the  $W_i$  and  $v_i$  are the weights and biases of the dense hidden layers. The models were trained using MSE loss.

### 3.4 Dense network on PCA augmented with external parameters (Dense-PCAX)

In [23], the values of the initial thickness  $h'_0$ , initial fluorescein concentration  $f'_0$ , and observation time length  $t'_s$  are all determined by processes external to the inverse problem for the ODE, which optimized for the remaining parameters describing the evaporation rate and flow.

Our ODE and PDE models produce training data by varying over both types of parameters without making a distinction. In order to determine whether forecasting ability improves when given access to exactly the same data as the ODE inverse problem in [23], we ran a variant of Dense-PCA in which the PCA component vector  $x$  in (9) was concatenated with the values of  $h'_0$ ,  $f'_0$ , and  $t'_s$ , which are included as inputs to the learner.

## 4 Results

As described in [section 3](#), the two mathematical models each generated a synthetic dataset for three ML learning models. For the input training set  $\mathcal{I}_{\text{tr}}$ , 4 PCA components were sufficient to achieve reconstruction mean squared error (MSE) of

Model	Input	Output	Hidden layers
FFN	601	601	300, 200, 200
Dense-PCA	4	4 (ODE) / 13 (PDE, $c$ ) / 8 (PDE, $h$ )	300, 300, 300
Dense-PCAX	7	4 (ODE) / 13 (PDE, $c$ ) / 8 (PDE, $h$ )	300, 300, 300

**Table 5:** Neural network layer sizes used for our results.

approximately  $1.4 \times 10^{-4}$ . For the output training sets, the number of components needed for comparable reconstruction varied by mathematical model and output variable. The sizes of all the layers in the ML learners are summarized in [Table 5](#). Each learner was trained for 1000 epochs using the Adam optimizer with a learning rate of 0.001.

Each type of learner was tested on two prediction tasks for both thickness  $h$  and osmolarity  $c$ :

*Synthetic:* Test the learner on its own (synthetic) testing set. This task evaluates how well the ML learner captures the full range of the mathematical model in the context of the mapping from FL intensity to thickness and osmolarity.

*Experimental:* The 467 intensity time series of presumed TBU that were fit in [\[23\]](#) to the ODE model using traditional inverse problem optimization form an additional testing set.

Our results report relative root-mean-square error (rRMSE), defined for a prediction  $\hat{y}$  of time series vector  $y$  by

$$\text{RMSE}_y = \left[ \frac{1}{N} \sum_{k=1}^N (y_k - \hat{y}_k)^2 \right]^{1/2},$$

$$\text{rRMSE}_y = \frac{\text{RMSE}_y}{\left( \frac{1}{N} \sum_{k=1}^N y_k^2 \right)^{1/2}}.$$

#### 4.1 Synthetic data

[Figure 2](#) shows the distributions of rRMSE of both  $h$  and  $c$  for all three ODE-trained learners on the synthetic test set. Thickness  $h$  was predicted to at least one digit of accuracy in nearly all cases, as was  $c$  for FFN and Dense-PCA. Compared to FFN, the PCA model was somewhat better at prediction for osmolarity, while the accuracy for thickness was similar. [Figure 3](#) compares the individual ODE-trained predictions of the final-time osmolarity  $c(1)$  to the actual values in the synthetic test set. Here we see that the poor performance of Dense-PCAX is due to underestimation when  $c(1) > 8$ .

[Figure 4](#) shows the rRMSE values of osmolarity and thickness of the PDE-trained models on the PDE test data. All perform similarly for osmolarity, while for thickness, Dense-PCAX outperforms Dense-PCA slightly, which is a little better than FFN. [Figure 5](#) shows the predictions of final osmolarity, where Dense-PCA shows more variance than the other two learners. The task is most difficult for all three models when  $c(1)$  is large.

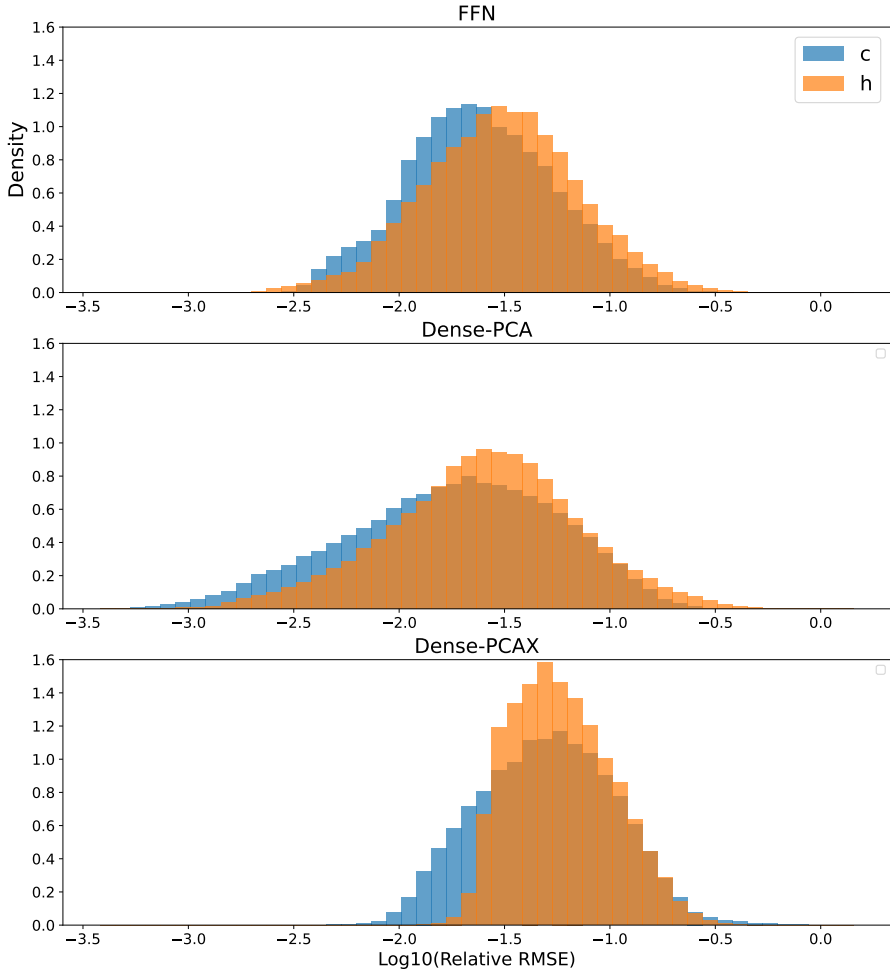


**Fig. 2:** Relative RMSE for synthetic testing of ML models trained by ODE data. Top to bottom: FFN, Dense-PCA, Dense-PCAX.

## 4.2 Experimental data

Driscoll et al. [23] fit 467 intensity time series of presumed TBU to the ODE model using traditional inverse problem optimization, thereby producing solutions  $h$  and  $c$  consistent with the observed intensity. Our ML models are meant to accomplish the same predictions without reference to the mathematical models once trained.

Note that only cases for which a good ODE fit was found were reported in that work, introducing a form of bias, and that the possible existence of fits to  $I$  nearly as good with different predictions of  $h$  and  $c$  is unknown. Moreover, while the ODE-trained predictors have learned the dynamics from the same mathematical models as in [23], the PDE-trained predictors have a presumably more physically realistic picture of the dynamics. Thus, while we continue to report "errors" in the following

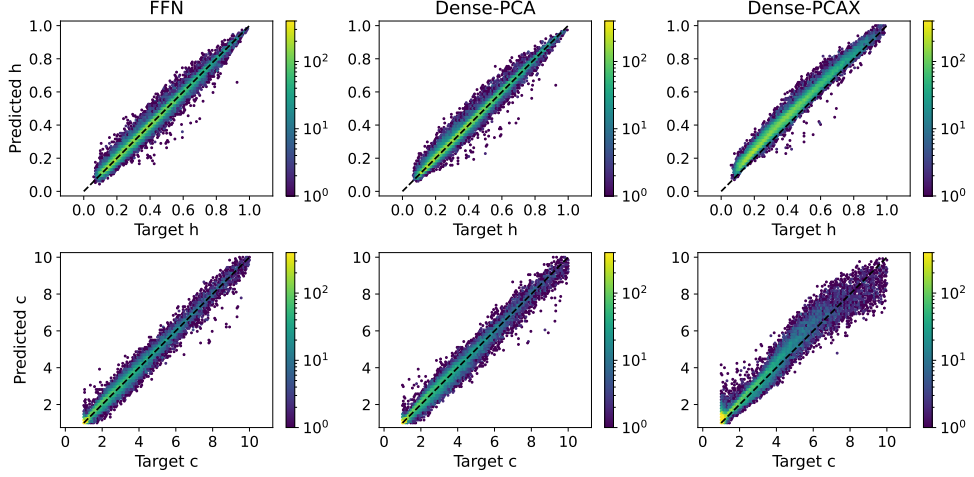


**Fig. 3:** Two-dimensional histograms showing counts of predictions by ODE-trained learners on the synthetic ODE testing data. First row: predictions of final thickness. Second row: predictions of final osmolarity.

results with respect to [23] as reference values, they might better be described as “discrepancies” for the PDE predictions.

Figure 6 shows the rRMSE of predictions by the ODE-trained models on the experimental data, while Figure 7 shows the errors for PDE-trained models. For ODE predictions, the Dense-PCAX is a little worse than the others for thickness but slightly better for osmolarity. All three PDE models are similar to one another; the PDE models show less agreement with reference thickness predictions but much greater agreement on osmolarity.

Figure 8 shows the dependence of rRMSE on the ODE fit parameters  $b_1$  and  $J_e$ , which are proxies for shear flow rate and evaporation rate. The ODE-trained predictors show the greatest discrepancies in osmolarity for large  $b_1 > 0$  and small  $J_e$ —that is, flow-dominated thinning—while the greatest discrepancies in thickness are for large  $J_e$  and  $b_1 < 0$ , which indicates strong evaporation with resultant inward flow. For the PDE-trained predictor, osmolarity shows the same pattern as for the ODE-trained model, while thickness discrepancy is largest for moderate outward flow over a wide range of evaporation rates.

Finally, Figure 9 shows the predictions of minimum thickness and maximum osmolarity for the reference data and the best ODE-trained and PDE-trained learners. The distribution of minimum thickness is similar for the ODE predictor and reference, but the reference predicts far more cases of maximum osmolarity staying close to 1. The PDE predictor is much more likely to predict minimum thickness greater than 0.75 and a moderately larger maximum osmolarity on average.

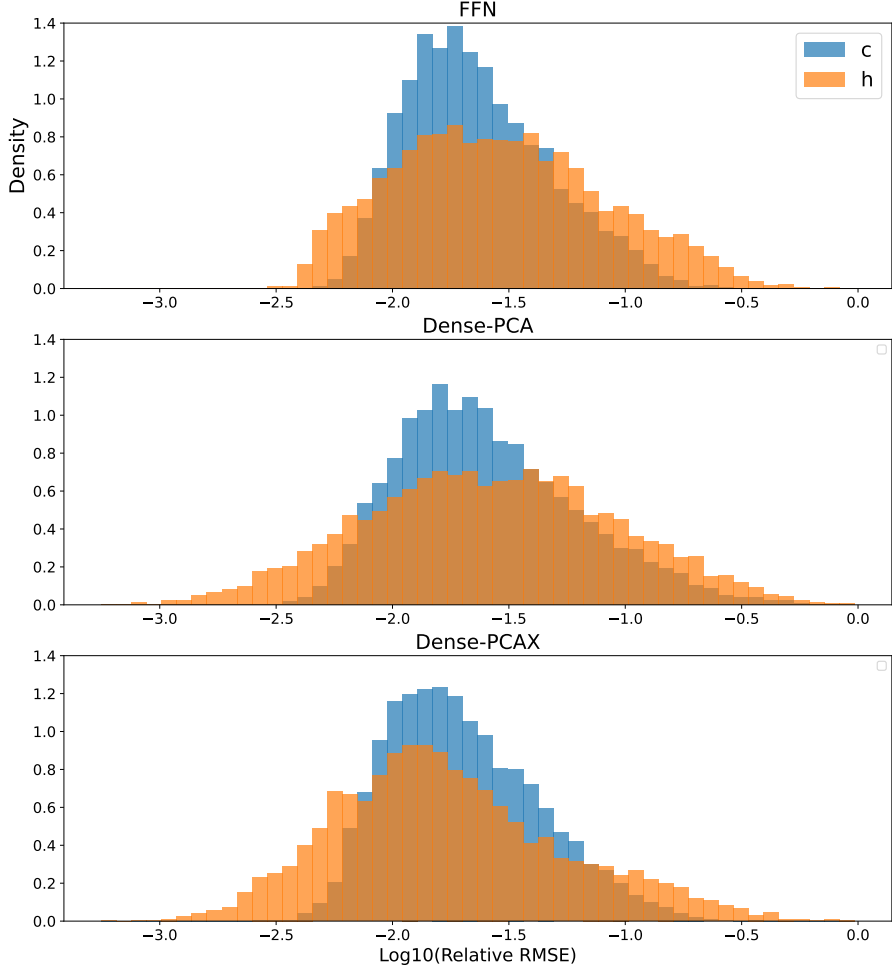


**Fig. 4:** Relative RMSE for synthetic self-consistency testing of ML models trained by PDE data. Top to bottom: FFN, Dense-PCA, Dense-PCAX.

## 5 Discussion

Multiple operator learning methods were trained on datasets comprising simulations of ODE models and of PDE models. Performance, as measured on synthetic test data, did not depend strongly on the particular learning method or architecture used—broadly speaking, 1-2 digits of normwise accuracy were found in most cases. Given that each training set was generated from a six-dimensional parameter space, and the weak dependence on the learning method, we speculate that the accuracy of the predictions is limited mainly by the nature of the underlying mapping from a single-spot fluorescent intensity time series to thickness and osmolarity—that is, by the inherent identifiability of the dependent quantities on FL data presented in this form.

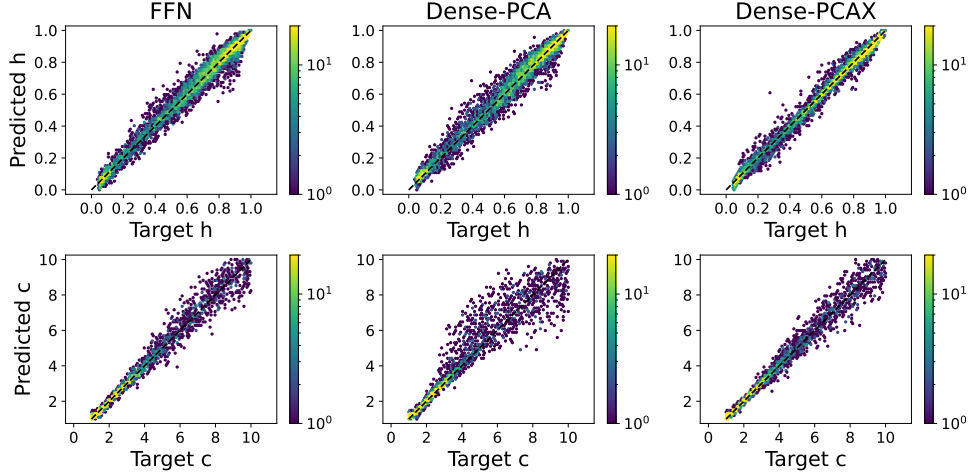


**Fig. 5:** Two-dimensional histograms showing counts of predictions by PDE-trained learners on the synthetic PDE testing data. First row: Predictions of final thickness. Second row: Predictions of final osmolarity.

Compared to the inverse problem predictions of [23] on experimental data, the ML predictions based on the same ODE model are much less likely to predict minor change in osmolarity simultaneously with substantial thinning, and large osmolarity simultaneously with little thinning. Differences in osmolarity predictions appear most often in what [23] describes as flow-dominated, zero-evaporation instances, while differences in thickness predictions also occur for strongly evaporative instances. One possibility is that the standard ODE inverse problem can be more easily induced to produce solution types that play a small role in the full solution set. Since the underlying physical realities are unknown, we cannot determine whether such results represent appropriate inverse problem responses or a manifestation of overfitting in the standard inverse problem.

On experimental data, the PDE-trained models predict much less thinning on average than either of the ODE-based predictors do over a wide range of evaporation rates. This suggests a fundamental difference between the ODE and PDE models of the phenomenon. While the PDE predictions have even fewer cases than the ODE learners of osmolarity remaining very close to 1, they do make more predictions between 1.25 and 1.75 and thus are distributed more like the inverse problem reference results.

It is plausible that PDE-trained models would perform better, at least on synthetic data, if the training data included information from more than a single location per observation. This would substantially increase the size of inputs and outputs to the learners, increasing training times. We also note that the learners in this work have no constraints from physics or dynamics other than what is implied by the training data. Methods that can incorporate such information, such as physics-informed neural nets [46, 47], neural ODEs [48, 49], and universal differential equations [50] might be expected to perform better.

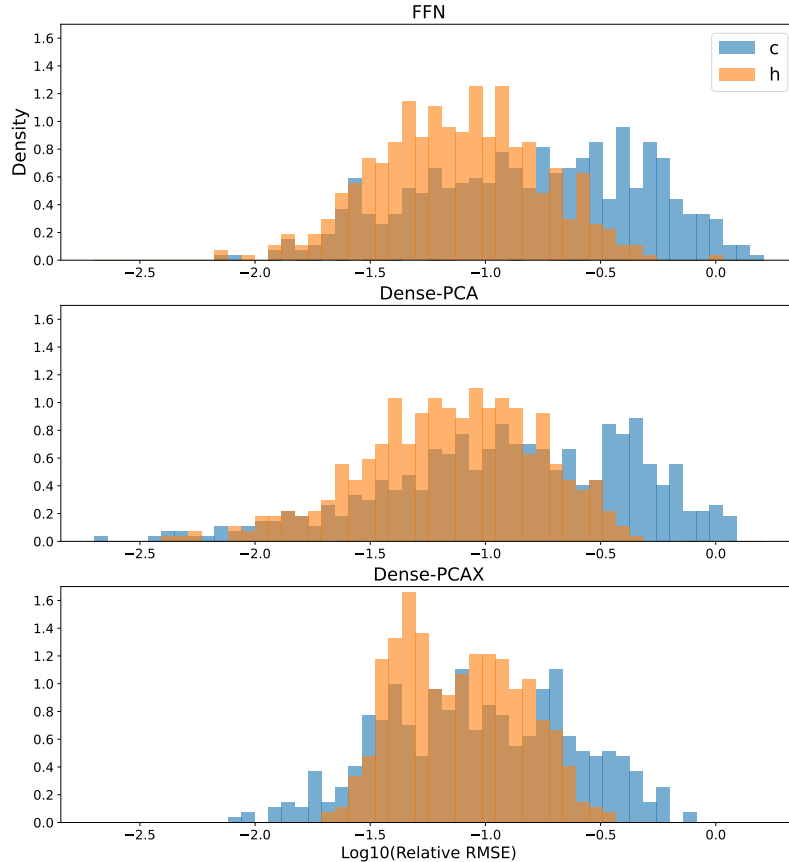


**Fig. 6:** Relative RMSE for ODE-trained learners on the experimental data.

**Conflict of Interest.** The authors declare no competing interests.

## References

- [1] Doane, M.G.: Interaction of eyelids and tears in corneal wetting and the dynamics of the normal human eyeblink. *Am. J. Ophthalmol.* **89**, 507–516 (1980)
- [2] Willcox, M.D.P., Argüeso, P., Georgiev, G.A., Holopainen, J.M., Laurie, G.W., Millar, T.J., Papas, E.B., Rolland, J.P., Schmidt, T.A., Stahl, U., Suarez, T., Subbaraman, L.N., Uçakhan, O.Ö., Jones, L.: TFOS DEWS II Tear Film Report. *Ocul. Surf.* **15**(3), 366–403 (2017)
- [3] Braun, R.J., King-Smith, P.E., Begley, C.G., Li, L., Gewecke, N.R.: Dynamics and function of the tear film in relation to the blink cycle. *Prog. Ret. Eye Res.* **45**, 132–164 (2015)

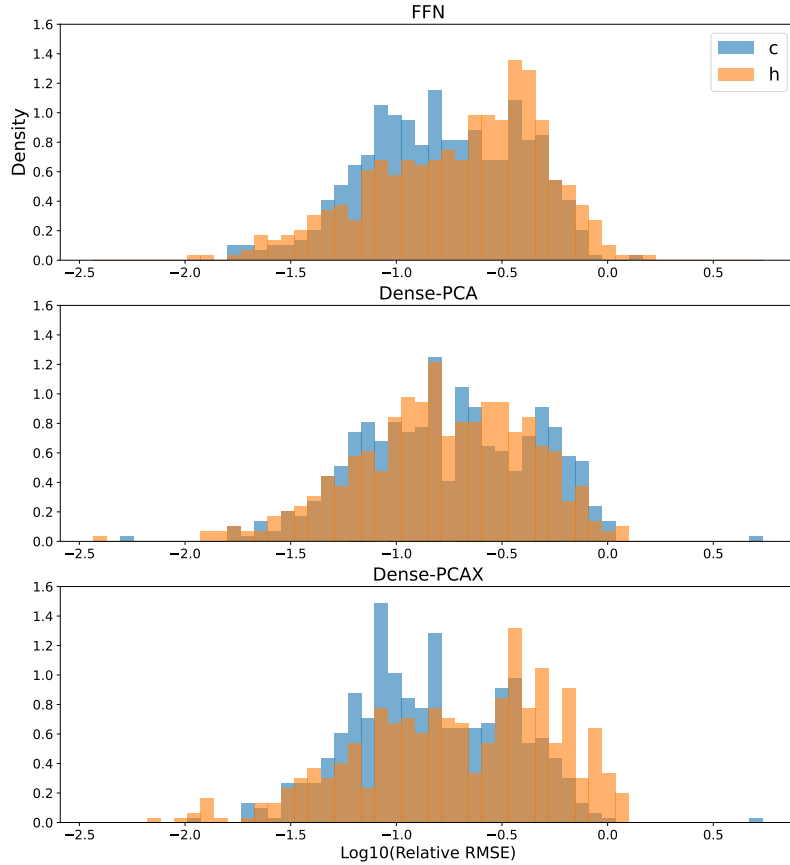


**Fig. 7:** Relative RMSE for PDE-trained learners on the experimental data.

- [4] Holly, F.J.: Formation and rupture of the tear film. *Exp. Eye Res.* **15**(5), 515–525 (1973)
- [5] King-Smith, P.E., Fink, B.A., Hill, R.M., Koelling, K.W., Tiffany, J.M.: The thickness of the tear film. *Curr. Eye Res.* **29**(4-5), 357–368 (2004)
- [6] Mishima, S., Maurice, D.M.: The oily layer of the tear film and evaporation from the corneal surface. *Exp. Eye Res.* **1**, 39–45 (1961)
- [7] Gipson, I.K.: Distribution of mucins at the ocular surface. *Exp. Eye Res.* **78**(3), 379–388 (2004)
- [8] Dartt, D.A.: Neural regulation of lacrimal gland secretory processes: Relevance in dry eye diseases. *Prog. Ret. Eye Res.* **28**(3), 155–177 (2009)
- [9] Braun, R.J.: Dynamics of the Tear Film. *Annu. Rev. Fluid Mech.* **44**(1), 267–297

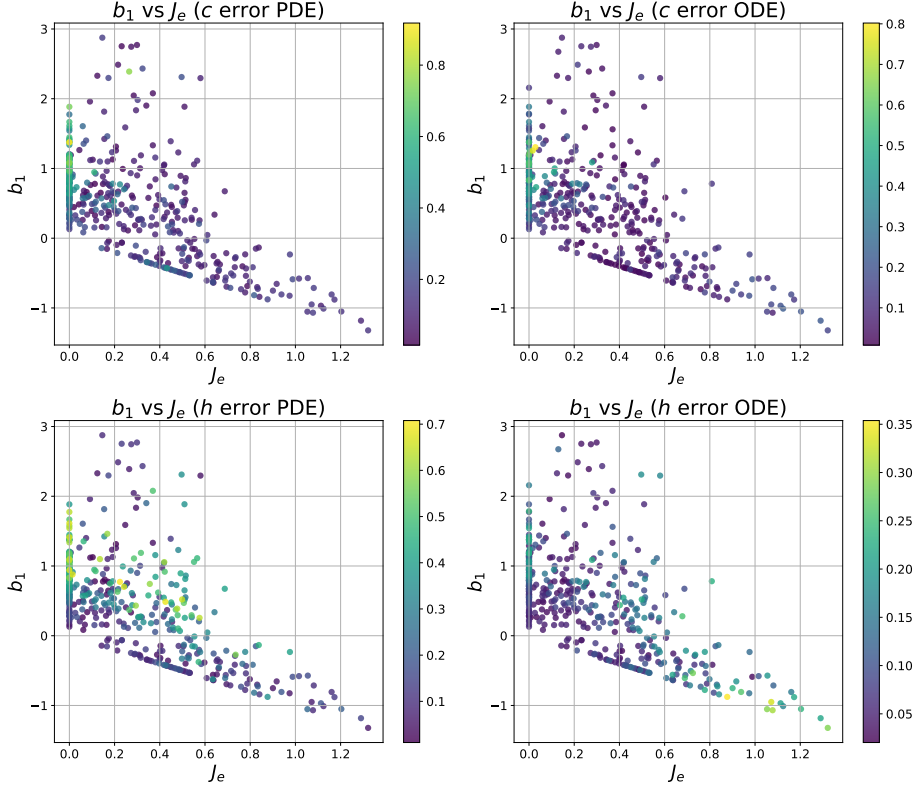


**Fig. 8:** By rows: osmolarity error to thickness error; By columns: PDE Dense-PCAX model to ODE Dense-PCAX model. Color indicates the error comparing to the calculated values, shown as functions of the nondimensional ODE parameters  $J_e$ ,  $b_1$ .

(2012)

- [10] King-Smith, P.E., Begley, C.G., Braun, R.J.: Mechanisms, imaging and structure of tear film breakup. *The ocular surface* **16**(1), 4–30 (2018)
- [11] Lemp, M.A.: The definition and classification of dry eye disease: Report of the Definition and Classification Subcommittee of the International Dry Eye WorkShop (2007). *Ocul. Surf.* **5**(2), 75–92 (2007)
- [12] Nelson, J.D., Craig, J.P., Akpek, E.K., Azar, D.T., Belmonte, C., Bron, A.J., Clayton, J.A., Dogru, M., Dua, H.S., Foulks, G.N., Gomes, J.A.P., Hammitt, K.M., Holopainen, J., Jones, L., Joo, C.-K., Liu, Z., Nichols, J.J., Nichols, K.K., Novack, G.D., Sangwan, V., Stapleton, F., Tomlinson, A., Tsubota, K., Willcox, M.D.P., Wolffsohn, J.S., Sullivan, D.A.: TFOS DEWS II Introduction. *Ocul. Surf.* **15**(3), 269–275 (2017)

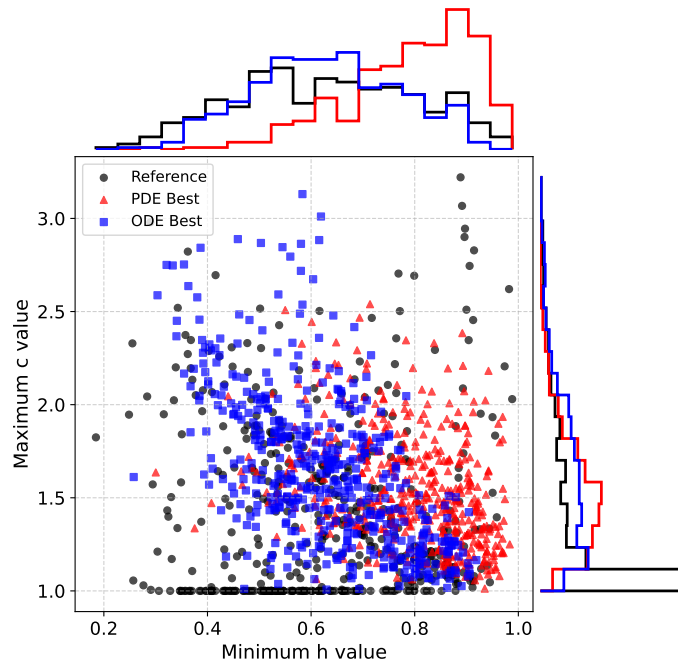


**Fig. 9:** Predictions of maximum osmolarity and minimum thickness for the reference [23] (black circles) and two ML models (red triangles for PDE training, blue squares for ODE training). The top and right histograms show the marginal distributions of thickness and osmolarity, respectively.

- [13] Stapleton, F., Alves, M., Bunya, V.Y., Jalbert, I., Lekhanont, K., Malet, F., Na, K.-S., Schaumberg, D., Uchino, M., Vehof, J., Viso, E., Vitale, S., Jones, L.: TFOS DEWS-II epidemiology report. *Ocul. Surf.* **15**(3), 334–365 (2017)
- [14] Lin, H., Yiu, S.C.: Dry eye disease: A review of diagnostic approaches and treatments. *Saudi J. Ophthalmol.* **28**(3), 173–181 (2014)
- [15] Baudouin, C., Aragona, P., Messmer, E.M., Tomlinson, A., Calonge, M., Boboridis, K.G., Akova, Y.A., Geerling, G., Labetoulle, M., Rolando, M.: Role of hyperosmolarity in the pathogenesis and management of dry eye disease: Proceedings of the OCEAN group meeting. *Ocul. Surf.* **11**, 246–258 (2013)
- [16] Norn, M.S.: Micropunctate Fluorescein Vital Staining of the Cornea. *Acta Ophthalmol.* **48**(1), 108–118 (1970)

- [17] Peng, C.-C., Cerretani, C., Braun, R.J., Radke, C.J.: Evaporation-driven instability of the precorneal tear film. *Adv. Coll. Interface Sci.* **206**, 250–264 (2014)
- [18] Braun, R.J., Driscoll, T.A., Begley, C.G., King-Smith, P.E., Siddique, J.I.: On tear film breakup (TBU): Dynamics and imaging. *Math. Med. Biol.: A Journal of the IMA* **35**(2), 145–180 (2018)
- [19] Zhong, L., Braun, R.J., Begley, C.G., King-Smith, P.E.: Dynamics of Fluorescent Imaging for Rapid Tear Thinning. *Bull. Math. Biol.* **81**(1), 39–80 (2019)
- [20] Luke, R.A., Braun, R.J., Driscoll, T.A., Begley, C.G., Awisi-Gyau, D.: Parameter Estimation for Evaporation-Driven Tear Film Thinning. *Bull. Math. Biol.* **82**(6), 71 (2020)
- [21] Luke, R.A., Braun, R.J., Driscoll, T.A., Awisi-Gyau, D., Begley, C.G.: Parameter Estimation for Mixed-Mechanism Tear Film Thinning. *Bull. Math. Biol.* **83**(5), 56 (2021)
- [22] Luke, R.A., Braun, R.J., Driscoll, T.A., Sinopoli, D., Yawatkar, V., You, L., Phatak, A., Begley, C.G.: Fitting Simplified Models to Machine Learning-Identified Tear Film Breakup. *Invest. Ophthalmol. Vis. Sci.* **62**(8), 1315–1315 (2021)
- [23] Driscoll, T.A., Braun, R.J., Luke, R.A., Sinopoli, D., Phatak, A., Dorsch, J., Begley, C.G., Awisi-Gyau, D.: Fitting ODE models of tear film breakup. *Model. Artif. Intell. Ophthalmol.* **5**, 1–36 (2023)
- [24] Ji, H., Witelski, T.P.: Finite-time thin film rupture driven by modified evaporative loss. *Physica D: Nonlinear Phenomena* **342**, 1–15 (2017)
- [25] Shi, X., Fuller, G.G., Shaqfeh, E.S.G.: Instability and symmetry breaking of surfactant films over an air bubble. *J. Fluid Mech.* **953**, 26 (2022)
- [26] Chen, Q., Driscoll, T.A., Braun, R.J.: Evaporation-driven tear film thinning and breakup in two space dimensions. *Journal of Engineering Mathematics* **149**(1), 5 (2024) <https://doi.org/10.1007/s10665-024-10407-6>
- [27] Chen, Q., Driscoll, T.A.: Parameter Estimation for an Evaporation-Driven Tear Film Model in Two Space Dimensions. in preparation
- [28] Chen, C., Wu, J.-L.: Operator Learning for Continuous Spatial-Temporal Model with A Hybrid Optimization Scheme. *arXiv* (2023). <https://doi.org/10.48550/arXiv.2311.11798>
- [29] Wang, S., Wang, H., Perdikaris, P.: On the Eigenvector Bias of Fourier Feature Networks: From Regression to Solving Multi-Scale PDEs with Physics-Informed

Neural Networks. Elsevier (2021). <https://doi.org/10.1016/j.cma.2021.113938> .  
<https://doi.org/10.1016/j.cma.2021.113938> Accessed 2025-06-05

- [30] Tancik, M., Srinivasan, P., Mildenhall, B., Fridovich-Keil, S., Raghavan, N., Singhal, U., Ramamoorthi, R., Barron, J., Ng, R.: Fourier Features Let Networks Learn High Frequency Functions in Low Dimensional Domains. In: Advances in Neural Information Processing Systems, vol. 33, pp. 7537–7547. Curran Associates, Inc., Red Hook, NY, USA (2020)
- [31] Lanthaler, S.: Operator learning with pca-net: upper and lower complexity bounds. *Journal of Machine Learning Research* **24**(318), 1–67 (2023)
- [32] Tiffany, J.M.: The viscosity of human tears. *Internat. Ophthalmol.* **15**(6), 371–376 (1991)
- [33] Nagyová, B., Tiffany, J.M.: Components responsible for the surface tension of human tears. *Current Eye Research* **19**(1), 4–11 (1999)
- [34] Ajaev, V.S., Homsy, G.M.: Steady vapor bubbles in rectangular microchannels. *Journal of Colloid and Interface Science* **240**(1), 259–271 (2001) <https://doi.org/10.1006/jcis.2001.7562>
- [35] Casalini, T., Salvalaglio, M., Perale, G., Masi, M., Cavallotti, C.: Diffusion and aggregation of sodium fluorescein in aqueous solutions. *J. Phys. Chem.. B* **115**(44), 12896–12904 (2011)
- [36] Riquelme, R., Lira, I., Pérez-López, C., Rayas, J.A., Rodríguez-Vera, R.: Interferometric measurement of a diffusion coefficient: Comparison of two methods and uncertainty analysis. *J. Phys. D: Appl. Phys.* **40**(9), 2769–2776 (2007)
- [37] Lemp, M.A., Bron, A.J., Baudouin, C., Benítez Del Castillo, J.M., Geffen, D., Tauber, J., Foulks, G.N., Pepose, J.S., Sullivan, B.D.: Tear osmolarity in the diagnosis and management of dry eye disease. *Am.J. Ophthalmol.* **151**(5), 792–7981 (2011)
- [38] Mota, M.C., Carvalho, P., Ramalho, J., Leite, E.: Spectrophotometric analysis of sodium fluorescein aqueous solutions. Determination of molar absorption coefficient. *Internat. Ophthalmol.* **15**(5), 321–326 (1991)
- [39] Webber, W.R., Jones, D.P.: Continuous fluorophotometric method of measuring tear turnover rate in humans and analysis of factors affecting accuracy. *Med. Biol. Eng. Comput.* **24**(4), 386–392 (1986)
- [40] Braun, R.J., Gewecke, N.R., Begley, C.G., King-Smith, P.E., Siddique, J.I.: A Model for Tear Film Thinning With Osmolarity and Fluorescein. *Invest. Ophthalmol. Vis. Sci.* **55**(2), 1133–1142 (2014)

- [41] Wu, Z., Begley, C.G., Port, N., Bradley, A., Braun, R., King-Smith, E.: The Effects of Increasing Ocular Surface Stimulation on Blinking and Tear Secretion. *Invest. Ophthalmol. Vis. Sci.* **56**(8), 4211–4220 (2015)
- [42] Trefethen, L.N.: Spectral Methods in Matlab. Software, Environments, Tools. SIAM, Philadelphia (2000)
- [43] Rackauckas, C., Nie, Q.: Differentialequations.jl—a performant and feature-rich ecosystem for solving differential equations in julia. *Journal of Open Research Software* **5**(1), 15 (2017)
- [44] Wang, S., Wang, H., Perdikaris, P.: On the eigenvector bias of fourier feature networks: From regression to solving multi-scale pdes with physics-informed neural networks. *Comput. Methods Appl. Mech. Eng.* **384**, 113938 (2021)
- [45] Yadav, S.: Combining pca with neural networks: Improving model efficiency and interpretability. *Int. J. Innov. Res. Eng. Multidiscip. Phys. Sci.* **7**, (2019)
- [46] Cuomo, S., Di Cola, V.S., Giampaolo, F., Rozza, G., Raissi, M., Piccialli, F.: Scientific Machine Learning Through Physics-Informed Neural Networks: Where we are and What's Next. *Journal of Scientific Computing* **92**(3), 88 (2022) <https://doi.org/10.1007/s10915-022-01939-z>
- [47] Li, Z., Zheng, H., Kovachki, N., Jin, D., Chen, H., Liu, B., Azizzadenesheli, K., Anandkumar, A.: Physics-Informed Neural Operator for Learning Partial Differential Equations. arXiv (2023). <https://doi.org/10.48550/arXiv.2111.03794>
- [48] Chen, R.T.Q., Rubanova, Y., Bettencourt, J., Duvenaud, D.: Neural Ordinary Differential Equations. arXiv (2019). <https://doi.org/10.48550/arXiv.1806.07366>
- [49] Kidger, P.: On Neural Differential Equations. arXiv (2022). <https://doi.org/10.48550/arXiv.2202.02435>
- [50] Rackauckas, C., Ma, Y., Martensen, J., Warner, C., Zubov, K., Supekar, R., Skinner, D., Ramadhan, A.: Universal Differential Equations for Scientific Machine Learning. arXiv:2001.04385 [cs, math, q-bio, stat] (2020) [arxiv:2001.04385](https://arxiv.org/abs/2001.04385) [cs, math, q-bio, stat]